

Multi-band Variability of the TeV Blazar PG 1553+113 with *XMM-Newton*

Vinit Dhiman^{1,2*}, Alok C. Gupta^{1†}, Haritma Gaur^{1‡}, Paul J. Wiita³

¹*Aryabhata Research Institute of Observational Sciences (ARIES), Manora Peak, Nainital 263001, India*

²*School of Studies in Physics & Astrophysics, Pt. Ravishankar Shukla University, Amanaka G.E. Road, Raipur 492010, India*

³*Department of Physics, The College of New Jersey, PO Box 7718, Ewing, NJ 08628-0718, USA*

28 June 2021

ABSTRACT

We present variability analyses of twenty pointed *XMM-Newton* observations of the high energy peaked TeV blazar PG 1553+113 taken during 2010 to 2018. We found intraday variability in the total X-ray energy range (0.3 – 10 keV) in 16 out of 19 light curves or a duty cycle of $\sim 84\%$. A discrete correlation function analysis of the intraday light curves in the soft and hard X-ray bands peaks on zero lag, showing that the emission in hard and soft bands are co-spatial and emitted from the same population of leptons. Red-noise dominates the power spectral density (PSD) of all the LCs although the PSDs have a range of spectral slopes from -2.36 to -0.14 . On longer timescales, the optical and UV variability patterns look almost identical and well correlated, as are the soft and hard X-ray bands, but the optical/UV variations are not correlated to those in the X-ray band, indicating that the optical/UV and X-ray emissions are emitted by two different populations of leptons. We briefly discuss physical mechanisms which may be capable of explaining the observed flux and spectral variability of PG 1553+113 on these diverse timescales.

Key words: galaxies: active – BL Lacertae objects: individual: PG 1553+113

1 INTRODUCTION

Radio-loud active galactic nuclei (AGN) eject relativistic charged particle jets from their central supermassive black holes (SMBHs) which are in the mass range $10^6 - 10^{10} M_{\odot}$. Blazars are a subclass thereof, where one of the two-sided jets approaches the observer within an angle of $\lesssim 10^{\circ}$ to the line of sight (e.g., Urry & Padovani 1995). Blazar jets are capable of transporting large amounts of power in the forms of kinetic energy, radiation, and magnetic fields, from the vicinity of the central SMBH. Blazars are historically considered to be the combination of the BL Lacertae (BL Lac) objects, which show featureless spectra or very weak emission lines (equivalent width $EW \leq 5\text{\AA}$; Stocke et al. 1991; Marcha et al. 1996), and flat spectrum radio quasars (FSRQs) with prominent emission lines in their composite optical/UV spectrum (Blandford & Rees 1978; Ghisellini et al. 1997). The name “blazar” indicates that they show flux and often spectral variability across the entire electromagnetic (EM) spectrum. They are also characterised by core dominated radio structures, emit predominantly non-thermal radiation, and when measured, they evince strong polarisation in not only the radio but also optical bands (where $\geq 3\%$ qualifies as strong).

Since blazars emit radiation throughout the EM spectrum, simultaneous (or nearly so) multi-wavelength (MW) observations produce their spectral energy distributions (SEDs) in the energy range from radio through γ -rays, to at least GeV energies and sometimes to the very high TeV energies. The MW SEDs of blazars in a $\log(\nu F_{\nu})$ vs. $\log(\nu)$ representation show double-humped structures (Fossati et al. 1998) which are used to classify them as high synchrotron peaked (HSP), intermediate synchrotron peaked (ISP), or low synchrotron peaked (LSP) blazars. The first (low-energy) hump lies in IR to optical bands in LSPs (also called LBLs, or low frequency/energy BL Lacs) and in the far-ultraviolet to X-ray band in HSPs (high-frequency/energy BL Lac objects, or HBLs). The second (high-energy) hump peaks at GeV energies in LSPs and at TeV energies in HSPs. Based on the synchrotron peak frequency (ν_s), blazars classified into categories HSPs, ISPs, and LSPs, having $\nu_s > 10^{15}$ Hz, $10^{14} \text{ Hz} < \nu_s < 10^{15}$ Hz, and $\nu_s < 10^{14}$ Hz, respectively, (e.g., Abdo et al. 2010). The lower energy hump of the SED is clearly dominated by synchrotron radiation which originates from ultrarelativistic electrons in the jets but the origin of the high energy SED remains in question. According to leptonic models, the high energy portion of the SED can be explained by synchrotron photons (Synchrotron Self Compton, SSC) or external photons (External Compton, EC) gaining energy thorough inverse Compton (IC) scattering from the same electrons

* Email: dhiman@aries.res.in

† Email: acgupta30@gmail.com

‡ Email: harry.gaur31@gmail.com

that emit the synchrotron photons (e.g., Böttcher 2007). Alternate hadronic models for the high energy SED, in which the high energy photons are produced by the synchrotron emission from relativistic protons and/or the secondary charged pion decay process resulting from photon-hadronic interactions may be preferable for some sources (e.g., Mannheim 1993; Böttcher et al. 2013).

Flux variations in blazars that are observed to occur on rapid timescales, from a few minutes to less than a day, are commonly known as intraday variability (IDV) (Wagner & Witzel 1995) or microvariability (Miller et al. 1989) or intranight variability (Gopal-Krishna et al. 1993). Variations in flux between days and a few weeks is often called short term variability (STV), while the changes in flux observed over the course of a few months to several years are generally known as long term variability (LTV) (Gupta et al. 2004).

PG 1553+113 ($\alpha_{2000} = 15^{\text{h}} 55^{\text{m}} 43.04\text{s}$; $\delta_{2000} = +11^{\circ} 11' 24.36''$) at $z = 0.433$ (Danforth et al. 2010; Johnson et al. 2019) was first detected in the Palomar-Green (PG) survey of UV-excess stellar sources as a 15.5 mag blue stellar object (Green et al. 1986), and classified as BL Lac object by its featureless spectrum with an optical R magnitude varying from ~ 13 to ~ 15.5 mag (Miller & Green 1983). It is sometimes classified as an extreme HBL, based on the synchrotron peak position in its SED (Falomo & Treves 1990), and flux ratio of 5 GHz radio flux $F_{5\text{GHz}}$ and 2 keV X-ray flux $F_{2\text{keV}}$ which should be $\log(F_{2\text{keV}}/F_{5\text{GHz}}) \geq -4.5$ for that subclass (Rector et al. 2003). Values of $\log(F_{2\text{keV}}/F_{5\text{GHz}})$ from -4.99 to -3.88 have been measured for PG 1553+113 (Rector et al. 2003; Osterman et al. 2006).

VHE γ -ray emission above 200 GeV from PG 1553+113 was discovered using observations from the *High Energy Stereoscopic System* (H.E.S.S.) (Aharonian et al. 2006). This blazar has been observed on multiple other occasions with both the space-based *Fermi* and ground-based γ -ray telescopes e.g. *H.E.S.S.*, *MAGIC* (Major Atmospheric Gamma Imaging Cherenkov Telescopes), *VERITAS* (Very Energetic Radiation Imaging Telescope Array System), etc. (e.g., Albert et al. 2007, 2009; Aharonian et al. 2008; Abdo et al. 2010a; Aleksić et al. 2012; Aliu et al. 2015, and references therein). Its γ -ray emission is variable, which is typical for TeV blazars (Aleksić et al. 2015).

PG 1553+113 is a bright X-ray blazar as well and has been observed by several X-ray telescopes across large energy ranges, e.g., *Einstein*, *ROSAT*, *ASCA*, *BeppoSAX*, *RXTE*, *MAXI*, *XMM-Newton*, *Chandra*, *Swift*, *Suzaku*, and *NuSTAR* over many epochs in different flux states, but for most of these observations no evidence of rapid flux variability was noticed on IDV timescales (e.g., Reimer et al. 2008, and references within). However, one X-ray observation with *XMM-Newton* (out of 6 examined) showed rapid IDV on a time scale of around one hour (Raiteri et al. 2017). A Whole Earth Blazar Telescope (WEBT) multiwavelength campaign for the blazar PG 1553+113 was coordinated in 2013 during which the X-ray spectrum remained stable and a bluer-when-brighter trend in the optical region was found (Raiteri et al. 2015). An *RXTE* observational campaign found a doubling of the X-ray flux in 10 days and spectral curvature (Osterman et al. 2006). In a *Suzaku* observation, PG 1553+113 exhibited spectral curvature up to 30 keV, manifested as a softening with increasing energy so that the spectral shape could be described by either a broken power-law or a log-parabolic fit with equal statistical

goodness of fit (Reimer et al. 2008).

A search for multi-band optical flux and colour variations from PG 1553+113 on IDV timescales was performed and no such variations were noticed (Gaur et al. 2012). Extensive multi-band optical observations of PG 1553+113 were done during July 2013 – August 2014 using five telescopes in Asia and Europe. No genuine IDV in flux or colour was detected in any of these observations whereas clear LTV in flux and colour were detected in all bands in which observations were conducted (BVRI) (Gupta et al. 2016a). Recently multi-band optical flux and spectral variations of this BL Lac object were examined using observations carried out on 8 nights in April 2016 and only in one night IDV was detected in V and R band fluxes when a mean optical spectral index $\alpha_{\text{optical}} \sim 0.83 \pm 0.02$ with a maximum variation of 0.21 was found (Pandey et al. 2019). PG 1553+113 has a radio emitting jet extending at least 20 pc to the northeast (Rector et al. 2003). In VLBA interferometric observations at 22 GHz, the source showed a quiet compact-jet structure (Tiet et al. 2012; Piner & Edwards 2014). A marginal quasi-periodic oscillation (QPO) in PG 1553+113, of central period ~ 2.2 years in the observer's frame (1.48 years in the source frame) was suggested to be present in the γ -ray flux with observations done by *Fermi*-LAT (Ackermann et al. 2015). This possible QPO was supported by the presence of similar patterns in the radio and optical regimes (Ackermann et al. 2015), leading to even more attention to this source. A model invoking a binary system of SMBHs can explain this type of quasi-periodicity (Caproni et al. 2017). This campaign further continues in multiple wavelengths, but only five main peaks have been observed over nine years. Other possible origins of these peaks in the light curve are a helical jet model and a two jet model (Tavani et al. 2018).

We have been running an extensive X-ray IDV study of blazars for over a decade, using timing data from various X-ray telescopes, e.g. *XMM-Newton*, *Chandra*, *NuSTAR*, *Suzaku* (Gaur et al. 2010; Kalita et al. 2015; Bhagwan et al. 2016; Gupta et al. 2016b; Pandey et al. 2017, 2018; Aggrawal et al. 2018; Zhang et al. 2019). In blazars, and particularly in BL Lacs, the radiative emission is dominated by the Doppler boosted relativistic jet rather than the accretion disc. Unlike for radio IDV, where extrinsic interstellar scintillation plays a role (e.g. Quirrenbach et al. 1992), IDV in X-ray bands for blazars is an intrinsic phenomenon which may be explained by changes in the density of relativistic particles or irregularities in the magnetic field resulting from interaction with shocks and/or turbulent jets (Marscher 2014; Calafut & Wiita 2015). In general, LTV in blazars can be explained by the shock-in-jet model (Marscher & Gear 1985) along with geometric effects such as an overall bending of the jet. Under this project, we present here X-ray IDV, STV and multi-wavelength LTV studies of one the most observed TeV blazars, PG 1553+113, with observations taken by *XMM-Newton*. Although the above-mentioned and other other possible explanations for IDV for blazars in the X-ray band have been posited, there is no consensus on the physics underlying these fast variations. By gathering all of the data taken with *XMM-Newton*, most of which has not been examined for the presence of IDV, and subjecting it to a new and uniform analysis we are able to check whether or not this source actually frequently shows significant rapid X-ray variations. Further, we examine the power-spectra of those variations, when present. These analyses shed light on the physics of this emission, as discussed in Section 5.

The paper is structured as follows. Section 2 discusses the data selection from the *XMM-Newton* archive and the data reduction; in Section 3 we briefly describe the analysis techniques used. Results and discussion are provided in Section 4 and Section 5, respectively.

2 XMM-NEWTON ARCHIVAL DATA SELECTION AND REDUCTION

2.1 Data Selection Parameters

We selected the extreme TeV blazar PG 1553+113 from the TeV source catalogue (TeVCat¹). The source was observed by *XMM-Newton* on many occasions continuously for extended periods of time which is extremely useful for our study. The *XMM-Newton* satellite is capable of doing simultaneous observation in multiple energy bands and also has a large field of view (FOV). We took data from the European Photon Imaging Camera (EPIC) PN detector in the energy range (0.2–15 keV) and the Optical Monitor (OM) in the wavelength range (170nm–650nm). EPIC has three coaligned X-ray CCD-based instruments, EPIC-PN and two EPIC-MOS covering a 30 arcmin FOV (Strüder et al. 2001). The OM has three ultraviolet (UVW1, UVM2, UVW2) and three optical (V, U, B) filters with a 17 arcmin FOV (Mason et al. 2001), which provide simultaneous observations that allow us to test for correlations between X-ray, optical, and UV bands. We considered only the EPIC-PN data for our X-ray study because it is more sensitive and efficient than the EPIC-MOS detector (Strüder et al. 2001). In total, *XMM-Newton* made 22 observations of the source, taken between August 2010 – August 2018, and we downloaded the data of all these observation IDs from the HEASARC (High Energy Astrophysics Science Archive Research Centre) Data Archive.

We excluded those observations which have either poor image quality or a good time interval (GTI) of less than 20 ks. Using these selection criteria, we still had 20 extended observations for our study, in which the GTI ranges from 21.4 ks to 138.9 ks, binned into intervals of 200–500 s. The detailed observation log provided in Table 1 shows the total observing time was more than 450 h. For all of these 20 observation IDs, the OM observations were performed in all six filters, except for observation ID 0790381001 for which no data was available from the UVW2 filter. In every OM observation, each filter has two sets of exposure modes. One mode is imaging, in which the exposure time is 5000 seconds. The other mode is the fast one which has exposure times in the range of 3400–4400 seconds. The detailed observation log is provided in Table 1.

2.2 Data Reduction

We have used the standard procedure of the *XMM-Newton* Science Analysis System (SAS) version 16.1.0 to reprocess the Observation Data Files (ODF) and to calibrate the summary file with the updated Calibration Current File (CCF)². We used the *epchain* pipeline to generate the event file of the source. To check for high background soft-flares, we extracted light curves in the high energy range 10–12 keV taking the full-frame of the CCD and found flaring in some of the observation IDs. Next, we generated

GTI files where the count rate was less than 0.4 ct sec⁻¹, and these files contain information on free soft proton flares. We used the GTI files information and event files as input, and thus produced clean event files which are used to generate the X-ray light curves.

We used standard imaging mode data from the OM for our UV and optical studies. For the OM data reduction we used the standard SAS routine *omichain*, which is a *Perl* script. After reduction, we got a list of all objects which are present in the OM FOV. We then located our source and the corresponding source count rate and equivalent instrumental magnitude for further use.

2.3 Light Curve Generation

With the help of the clean event files, we generated a full-frame image of the CCD and selected a circular region of radii 30–45 arcsec centered around the source. These circular regions contain most of the point spread function (PSF). Since this blazar is a bright source, there is a real possibility of pileup, where there is a deficit of single events and an excess of double events. We therefore examined the pileup effect for each observation by using the *epatplot* SAS task and found pileup mainly in those observation IDs which have longer exposures. For pileup correction we follow the standard procedure and consider an annular region that excludes the overexposed central region in any observation ID³. So for those cases we use a central annulus with inner radius range of 7–12 arcsec instead of a circular region; the annular size that minimizes pileup for each observation is determined iteratively. A background region is selected within the same CCD chip on which the source is present and is taken to be a blank region of the same radius as the source and less affected by the source region. To get the source count we subtract this background noise level from the nominal measurement, which includes those extra counts. Using the *evselect* SAS task we applied the condition (PATTERN < 4) in the energy range 0.3–10 keV. Finally, we use *epicccorr* task and obtained the corrected event file. From this file we generated light curves (LCs). We made LCs in three different energy bands: 0.3–2.0 keV (soft X-ray band), 2.0–10 keV (hard X-ray band), and 0.3–0 keV (total X-ray band). A typical LC is shown in Fig. 1 and the other 19 are in Supplemental figures.

3 ANALYSIS TECHNIQUES

In this section we introduce various analysis methods and apply those to the data. The results obtained by these methods are discussed in the following Section 4.

3.1 Excess Variance

Blazars show rapid and strong flux variability over the whole electromagnetic (EM) spectrum on different time scales. Finite uncertainties $\sigma_{err,j}$ are produced in all N individual measured flux values of x_j in a LC due to the measurement error in the observations. An additional variance generated in the individual flux measurements, and due to these uncertainties, leads to the calculation of an excess variance σ_{XS}^2 which is the measure of the strength of variability in the source flux, and so can be considered to be the intrinsic source variance (Edelson et al. 2002;

¹ <http://tevcac.uchicago.edu/>

² <http://www.cosmos.esa.int/web/xmm-newton/sas-threads>

³ <https://www.cosmos.esa.int/web/xmm-newton/sas-thread-epatplot>

Table 1. Observation log of *XMM-Newton* X-ray data for PG 1553+113

Observation ID	Observation date	Filter	Window mode	Pileup	GTI (ks)	Bin Size (s)	OM Filter
0656990101	2010.08.06	Thin1	Small	No	21.4	200	1,2,3,4,5,6
0727780101	2013.07.24	Medium	Small	No	32.9	200	1,2,3,4,5,6
0727780201	2014.07.28	Medium	Small	No	34.7	200	1,2,3,4,5,6
0761100101	2015.07.29	Thin1	Full	Yes	130.3	500	1,2,3,4,5,6
0761100201	2015.08.02	Thin1	Full	Yes	123.0	500	1,2,3,4,5,6
0761100301	2015.08.04	Thin1	Full	Yes	135.8	500	1,2,3,4,5,6
0761100401	2015.08.08	Thin1	Full	Yes	133.5	500	1,2,3,4,5,6
0761100701	2015.08.16	Thin1	Small	Yes	88.4	300	1,2,3,4,5,6
0761101001	2015.08.30	Thin1	Full	Yes	127.0	500	1,2,3,4,5,6
0727780301	2015.09.04	Medium	Small	Yes	28.4	200	1,2,3,4,5,6
0727780401	2016.08.17	Medium	Small	Yes	28.4	200	1,2,3,4,5,6
0790380501	2017.02.01	Thin1	Full	Yes	56.8	300	1,2,3,4,5,6
0790380601	2017.02.05	Thin1	Full	Yes	132.3	500	1,2,3,4,5,6
0790380801	2017.02.07	Thin1	Full	Yes	134.3	500	1,2,3,4,5,6
0790380901	2017.02.11	Thin1	Full	Yes	135.2	500	1,2,3,4,5,6
0790381401	2017.02.13	Thin1	Full	Yes	138.4	500	1,2,3,4,5,6
0790381501	2017.02.15	Thin1	Full	Yes	138.9	500	1,2,3,4,5,6
0790381001	2017.02.21	Thin1	Small	Yes	95.5	500	1,2,3,4,5
0727780501	2017.08.22	Medium	Small	Yes	28.5	200	1,2,3,4,5,6
0810830101	2018.08.25	Medium	Small	Yes	33.2	200	1,2,3,4,5,6

Vaughan et al. 2003).

The fractional rms variability amplitude, F_{var} , which is the square root of the normalised excess variance, (Vaughan et al. 2003) is given by,

$$F_{var} = \sqrt{\frac{S^2 - \sigma_{err}^2}{\bar{x}^2}}, \quad (1)$$

in terms of the sample variance, S^2 , the mean square error, σ_{err}^2 , and the mean of the measurements, \bar{x} . Here we have used the expression of uncertainty in F_{var} from Vaughan et al. (2003)

$$(F_{var})_{err} = \sqrt{\left(\sqrt{\frac{1}{2n}} \frac{\sigma_{err}}{\bar{x}^2 F_{var}}\right)^2 + \left(\sqrt{\frac{\sigma_{err}^2}{n}} \frac{1}{\bar{x}}\right)^2}, \quad (2)$$

for n measurements.

3.2 Variability Timescale

To calculate the shortest flux variability time, we have used halving/doubling timescales from

$$F(t_1) = F(t_2)2^{(t_1-t_2)/\tau}, \quad (3)$$

where τ is a characteristic halving/doubling timescale and $F(t_1)$ and $F(t_2)$ are the fluxes of the LC at times t_1 and t_2 , respectively. Here we only consider changes where the differences in flux at t_1 and t_2 is greater than 3σ (Foschini et al. 2011). From the value of τ , we can estimate the size of X-ray emitting region.

3.3 Discrete Correlation Functions

The Discrete Correlation Function (DCF) analysis is used to find possible time-lags and cross-correlations between LCs of different energy bands. This technique was introduced by Edelson & Krolik (1988) and later modified by Hufnagel & Bregman (1992) to find better error estimates. In general, astronomical LCs are unevenly

binned, and, for such LCs this technique is very useful as it can be used for unevenly sampled data. Details about the computation of the DCF we employ here are provided in Pandey et al. (2017).

A DCF value > 0 indicates that there is some correlation between two data trains, with a value of $+1$ indicating a perfect correlation. A DCF value < 0 means that the data trains are anti-correlated, while if the DCF = 0 there is no correlation between them. When using the same data trains one has an auto-correlation function ACF with a guaranteed peak at $\tau = 0$ (or no time-lag) but other strong peaks in an ACF indicate a possible periodicity. Fuhrmann et al. (2014) and (Max-Moerbeck et al. 2014) demonstrated that DCF values should be considered critically and interpreted carefully, especially when the significance of the result is not estimated. Uncertainties in the data samples were estimated by a model independent Monte Carlo method (Peterson et al. 1998).

3.4 Hardness Ratio

A hardness ratio (HR) analysis provides a model-independent method for learning about spectral variations of the source. We divided the X-ray light curves into two energy bands: a soft one (0.3–2.0 keV) and a hard band (2.0–10 keV), and then calculated the hardness ratio (HR) as

$$HR = \frac{(H - S)}{(H + S)}. \quad (4)$$

Here S and H are the net counts s^{-1} in the soft and hard energy bands, respectively.

We used a standard χ^2 test for testing for spectral variations in the HR, evaluating,

$$\chi^2 = \sum_{k=1}^n \frac{(x_k - \bar{x})^2}{\sigma_k^2}. \quad (5)$$

Here \bar{x} is the mean value of HR, x_k is the HR value for the k^{th} data point, and σ_k is the corresponding error.

3.5 Duty Cycle

The duty cycle (DC) provides a direct estimation of the fraction of time for which a source has shown variability. We have estimated the DC of PG 1553+113 by using the standard approach (Romero et al. 1999). For these DC calculations, we considered only those LCs which were continuously monitored for at least about 6 hours, with

$$DC = 100 \frac{\sum_{i=1}^n N_i (1/\Delta t_i)}{\sum_{i=1}^n (1/\Delta t_i)} \text{ per cent} \quad (6)$$

here $\Delta t_i = \Delta t_{i,obs}(1+z)^{-1}$ is the redshift corrected GTI of the source observed having the i^{th} Observation ID, and N_i takes the value 1 whenever IDV is detected, and 0 when it is not; when the fractional variability amplitude, F_{var} is greater than 3 times $(F_{var})_{err}$, then we consider the LC to show genuine IDV. Computation of the DC has been weighted by the GTI Δt_i for the i^{th} observation ID, as the GTI is different for each observation.

3.6 Power Spectral Density

The power spectral density (PSD) shows the distribution of the variability power as a function of temporal frequency. The PSD is a form of periodogram analysis of LCs that allows for the characterization of the temporal variations in flux, including any exact periodicity or quasi-periodic oscillations (QPOs). In this method one first calculates the square of the Fourier transform of the given LC and then fits the red-noise variability of the PSD to a power-law. A significant QPO may be present whenever a peak in the PSD rises at least 3σ (99.73%) above the red-noise level of the PSD. To obtain the PSDs of these LCs we follow the procedure given by Vaughan (2005) as implemented in Zhang et al. (2019). We measured the Poisson (white) noise level of the power spectrum in the periodogram which causes the observed spectrum to flatten at high frequencies as the power in the red noise spectrum of the source becomes comparable to the power in the flat Poisson noise spectrum. Hence, we fit only the frequency range below which red noise dominates over the Poisson noise level. Using this recipe we found the PSDs; the unit of the periodogram is $(\text{rms}/\text{mean})^2 (\text{Hz})^{-1}$. In most variable AGNs, their PSDs can be characterized by a single power-law (although some are better fit by bending power-laws). We assume the former, and search for a relationship between the temporal frequency, ν , and the red-noise part of the PSD $P(\nu)$ of the power-law form $P(\nu) = N\nu^\alpha$, where N is the normalisation and α is the power-law spectral index ($\alpha \leq 0$) (van der Klis 1989), or the slope of the fit to logarithms of P and ν .

4 RESULTS

We now employ the various analysis methods discussed in Section 3 to the data described in Table 1 to find the following results.

4.1 Intraday X-ray Variability

In this section we discuss the results of our studies of the flux, spectral and cross-correlated X-ray variabilities of these 20 *XMM-Newton* extended observations of the source.

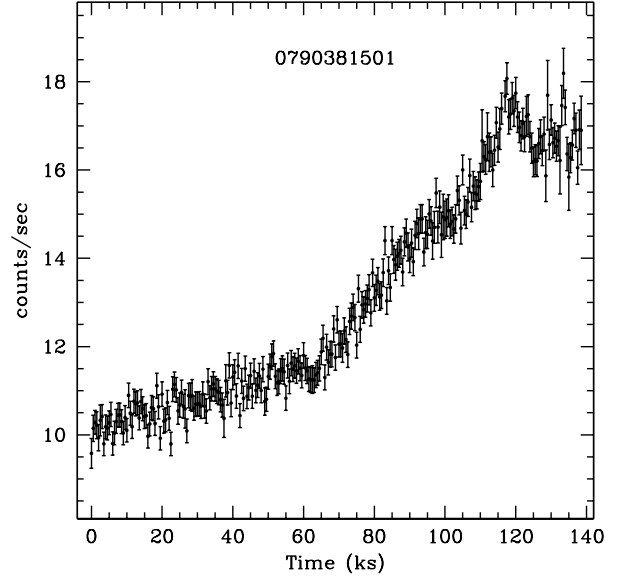


Figure 1. A sample *XMM-Newton* light curve of the TeV blazar PG 1553+113, labelled with its observation ID. The light curves for all observations appear in online supplemental material.

4.1.1 Flux Variability

We generated X-ray LCs for all the selected 20 observations: an exemplary LC of observation ID 0790381501 is shown in Fig. 1 and the remaining 19 LCs are displayed in online supplemental material. On visual inspection, only a few LCs show clear evidence of variability on these IDV timescales. To more fairly interrogate the variability on IDV timescales and to quantify their amplitudes, we have used the excess variance method briefly described in section 3.2, and the results obtained are reported in Table 2. We consider a LC variable only when the sample variance is more than the mean square error and the fractional amplitude variability, F_{var} , is greater than 3 times $(F_{var})_{err}$, following Paliya et al. (2015). With this definition we see that 16 out of 20 LCs show IDV (based on the entire X-ray band).

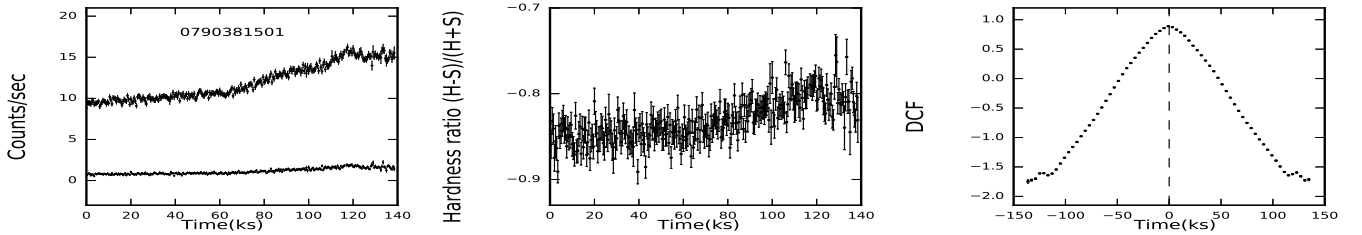
For further analysis, as mentioned above, we divided the whole X-ray energy range (0.3–10 keV) into two energy bands: soft (0.3–2 keV) and hard (2–10 keV) and plot them in the left panels of Figure 2, which shows an example of these LCs. We calculated F_{var} values and their errors in the hard and soft bands separately, as well as in the entire X-ray energy range, with results reported in Table 2. In the soft band, all of the 18 (out of 20) observations for which the sample variance is more than the mean square error of the observation ID show significant variability, as they also have $F_{var} > 3(F_{var})_{err}$. In the hard band the count rates are lower and only 14 of the 20 have sample variances exceeding the mean square error; of those, 10 also satisfy the criterion $F_{var} > 3(F_{var})_{err}$. However, when both bands show variations, the hard X-ray band variability is generally greater than the corresponding soft band (10 out of 13 cases). Two observations (IDs 0790380801 and 0790381501) show substantial large amplitude IDV, with $F_{var} > 18\%$.

In our analysis of the blazar PG 1553+113, we found the shortest X-ray flux observed doubling time to be 2.4 ± 0.7 ks for the

Table 2. X-Ray Variability and Timescale Parameters

Observation ID	$F_{var}(\%)$			Significance ^a	Variable	$ \tau ^b(\text{ks})$	$ \tau _{cor}^c(\text{ks})$
	Soft (0.3–2 keV)	Hard (2–10 keV)	Total (0.3–10 keV)				
0656990101	0.82±0.22	2.90±0.89	1.06±0.22	4.81	V	11.37± 3.27	7.63±2.40
0727780101 ^d	1.33±0.37	23.41± 7.39	15.71±5.38
0727780201	0.68±0.16	4.25	V	13.02± 3.19	8.74±2.38
0761100101	2.04±0.17	2.07±0.16	12.93	V	2.76± 0.79	1.85±0.58
0761100201	0.86±0.19	0.46±0.19	2.42	NV	5.64± 1.88	3.78±1.36
0761100301	2.40±0.18	0.59±0.59	2.24±0.17	13.18	V	2.86± 0.91	1.92±0.66
0761100401	0.90±0.19	1.69±0.66	0.25±0.19	1.32	NV	14.11± 3.55	9.47±2.64
0761100701	2.89±0.16	3.18±0.55	2.84±0.16	11.72	V	3.63± 1.16	2.43±0.84
0761101001	4.82±0.19	1.49±0.67	4.75±0.18	26.39	V	2.54± 0.65	1.70±0.48
0727780301	2.76±0.29	2.58±0.29	8.91	V	22.04± 6.17	14.79±4.54
0727780401	1.15±0.27	0.73±0.26	2.81	NV	33.31±10.58	22.35±7.69
0790380501	3.15±0.43	4.27±1.63	2.84±0.42	6.72	V	5.64± 1.72	3.78±1.26
0790380601	3.55±0.21	6.83±0.81	3.46±0.21	16.48	V	4.09± 1.28	2.75±1.22
0790380801	17.87±0.23	26.22±0.85	18.47±0.22	83.96	V	2.39± 0.69	1.61±0.50
0790380901	2.55±0.22	4.97±0.82	2.66±0.21	12.67	V	5.55± 1.80	3.73±1.31
0790381401	1.21±0.25	6.68±0.98	1.74±0.24	7.25	V	6.07± 1.85	4.08±1.35
0790381501	17.65±0.16	30.75±0.54	18.72±0.15	124.8	V	5.37± 1.54	3.60±1.13
0790381001	5.36±0.18	4.76±0.66	5.31±0.17	31.24	V	10.14± 3.31	6.81±2.40
0727780501	0.72±0.13	1.48±0.39	0.63±0.12	5.25	V	6.32± 1.98	4.24±1.45
0810830101	1.04±0.18	1.08±0.17	6.35	V	10.06± 2.79	6.75±2.05

Note: V= Variable NV= Non-variable

^a Significance = $F_{var}/(F_{var})_{err}$ for the total band^b $|\tau|$ = Observed halving/doubling time scale in ks^c $|\tau|_{cor}$ = Redshift corrected halving/doubling time scale: $|\tau|_{cor} = |\tau|/(1+z)$ ^d indicates that the variance arising from measurement error is greater than the total variance of the LC**Figure 2.** Soft energy (0.3–2 keV, upper plot, denoted by open circle) and hard energy (2– 10 keV, lower plot, denoted by asterisk) light curves for the TeV blazar PG 1553+113 (left panel) for a sample XMM-Newton observation ID 0790381501; corresponding hardness ratio (middle panel); discrete correlation function between those bands (right panel). Similar plots for all the observations appear in online supplemental material.

observation ID 0790380801. During three other observations the doubling times are comparably short (< 3 ks) and most of them are under 6.5 ks but in one of the observations (ID 0727780401) any doubling time is larger than the data length. These short doubling times are a key result and throughout the rest of the paper we will use the shortest doubling time of 2.4 ± 0.7 ks to estimate the various physical parameters related to this emission from the blazar.

4.1.2 Cross-correlated Variability

We have used the DCF technique to determine cross correlations and thus search for any time lags between the soft and hard X-ray energy bands for each of the observations of PG 1553+113. The DCF plot for the example LC is shown in the right panel of Figure 2 and in this case there is a strong correlation at 0 lag. However, presumably because the count rates in the hard band are usually so low and do not show obvious variations, only one more of the DCFs plotted in the supplemental figures yields a value above 0.5

at 0 lag, so in general, no correlations can be claimed. Still, for none of the LCs were there any significant DCF values at any non-zero time lags between the hard and soft bands. This result is consistent with the hypothesis that emission in both energy bands occurred at the same region and arose from the same population of leptons (Pandey et al. 2017), but by no means confirms it.

4.1.3 Spectral Variability

As a simple check for X-ray spectral variation on IDV timescales we looked for changes in the HR using a standard χ^2 test, as discussed in section 3.4. We considered spectral variation to be present for those observations in which $\chi^2 > \chi_{99,\nu}^2$, where ν is number of DOFs (degrees of freedom). The HRs as functions of time for individual observations are plotted for the example LCs in the middle panel of Figure 2. Three of these observations, all of which have large amplitude variability in fluxes, showed significant variations in HR with time; in all of those cases the spectra gets harder with an increase in brightness. However, the majority of the observations

did not show any significant HR variations, which is not surprising for situations where there are no large amplitude flux variations.

4.1.4 Duty Cycle

Our method of estimation of the DC is mentioned above. Based on the F_{var} test, we took the value of N_i as either 1 if variable, or 0 if not. In the whole X-ray energy band (0.3–10 keV) 16 out of 19 observations showed variability (as one LC had measurement errors exceeding the nominal variation). Using this approach we found the X-ray DC of this source to be $\sim 84\%$, illustrating that detectable IDV over this long time duration (2010–2018) was common. In an earlier analysis of a subset of 6 of these LCs Raiteri et al. (2017) only one was noted to show IDV, but with our approach two others would be considered as variable.

4.2 Power Spectral Density

To characterize the type of noise present in the variations on intraday timescales and to attempt to search for any QPOs over those spans, we performed PSD analyses of all 20 X-ray observations studied here. From the PSD plots (an example is shown in Fig. 3), we found all observations to have some degree of red-noise dominance and there is no sign of quasi-periodicity in any observation.

The slopes (α) of the PSDs are in the range of -0.14 ± 0.18 (essentially white noise) to -2.36 ± 0.25 steep, which is commonly seen in AGN X-ray variability (González-Martín & Vaughan 2012), and in some observations its value is ~ -1 (close to flicker noise). The values of the power-law slopes and normalisation constants for the all 20 observations are reported in Table 3. The normalisation constants are in the range of -9.24 ± 0.96 to -0.12 ± 0.51 for all observations, and the mean value of the PSD spectral index for PG 1553+113 is -1.21 ± 0.26 .

4.3 Short and Long Term Variability

In this section we discuss the flux and spectral variabilities on STV and LTV timescales by using all 20 *XMM-Newton* observations of the blazar PG 1553+113.

4.3.1 Short Term X-ray Flux Variability

We divide the complete set of observations into four different segments to study the X-ray STV nature of PG 1553+113 as shown in Figure 4. In panel (a), the first three average fluxes are displayed though they cover essentially the first four years. A denser sampling in panel (b) shows seven observations made over five weeks and in panel (c) seven observations were made in only three weeks. Panel (d) shows the last 2 observations, which were taken essentially a year apart. We omit plotting one data point taken on 17 August 2016 which has an average flux 13.74 ± 0.34 because it fell between the second and third grouping and had considerably larger gaps with both. The STV plots in all four panels of Fig. 4 show clear evidence of large flux variations on STV timescales. Considering all the measurements, the faintest to strongest total X-ray fluxes differ by a factor of 6.7.

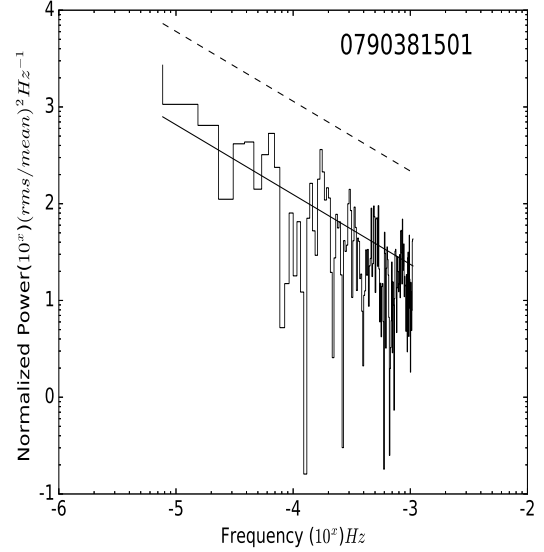


Figure 3. Power spectral density of the example X-ray light curve in the full energy range (0.3–10 keV), with the continuous line showing the fitted red-noise slope to the power spectral density and the dashed line showing a 3σ level above that noise; any measurements above that would provide a hint of a quasi periodic oscillation. These plots for all the observations appear in online supplemental material.

Table 3. Power-law fits to the PSDs^a of all 20 observations

Obs Ids	(α)	$\log(N)^b$
0656990101	-2.12 ± 0.16	-8.54 ± 0.65
0727780101	-1.13 ± 0.54	-5.54 ± 2.21
0727780201	-1.26 ± 0.54	-5.94 ± 2.09
0761100101	-1.22 ± 0.12	-2.99 ± 0.42
0761100201	-0.67 ± 0.11	-1.49 ± 0.38
0761100301	-0.81 ± 0.16	-1.51 ± 0.59
0761100401	-1.39 ± 0.10	-3.52 ± 0.38
0761100701	-1.91 ± 0.28	-7.77 ± 1.18
0761101001	-1.24 ± 0.11	-2.95 ± 0.38
0727780301	-2.36 ± 0.25	-9.24 ± 0.96
0727780401	-1.57 ± 0.45	-6.33 ± 1.75
0790380501	-0.93 ± 0.26	-1.06 ± 0.89
0790380601	-0.91 ± 0.15	-1.09 ± 0.53
0790380801	-1.21 ± 0.13	-2.32 ± 0.47
0790380901	-1.54 ± 0.25	-3.91 ± 1.04
0790381401	-1.43 ± 0.22	-3.41 ± 0.84
0790381501	-1.06 ± 0.17	-2.31 ± 0.62
0790381001	-0.64 ± 0.08	-1.56 ± 0.31
0727780501	-0.72 ± 0.26	-3.73 ± 0.89
0810830101	-0.14 ± 0.18	-0.12 ± 0.51

^a A power-law model is assumed with $P(f) \propto f^\alpha$ for $\alpha < 0$

^b Normalisation Constant, $(\text{rms}/\text{mean} \cdot \text{Hz})^2$

4.3.2 Long Term Multi-wavelength Flux Variability

We used all the data to analyse the long-term flux behaviour of the *XMM-Newton* satellite observations of PG 1553+113 over the period of 2010 to 2018 in optical and UV bands as well as in X-rays. We plot the fluxes in counts s^{-1} versus MJD for all the available bands in Figure 5 and calculated their fractional rms variability amplitudes, as discussed in section 3.1. Here we have estimated the rms variability amplitude (i.e., σ^2/m^2 where σ^2 and

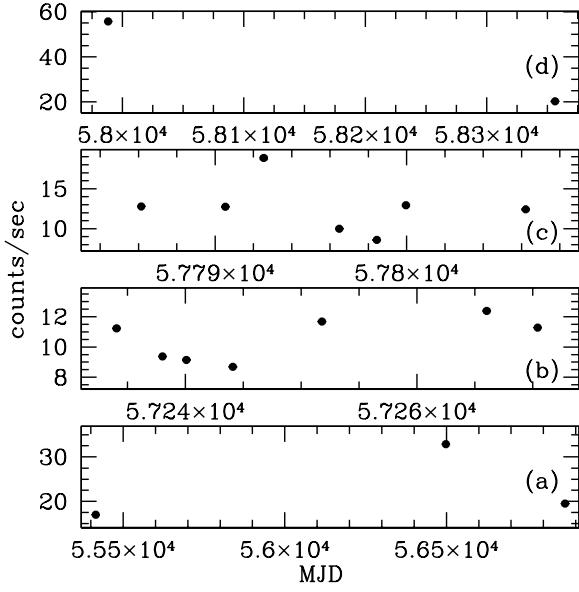


Figure 4. Short term variability plots in 0.3–10 keV. The observation spans are: (a) 6 August 2010 to 28 July 2014; (b) 29 July 2015 to 4 September 2015; (c) 1 – 21 February 2017; (d) observations taken on 22 August 2017 and 25 August 2018. Errors are not visible as they are smaller than the symbol size.

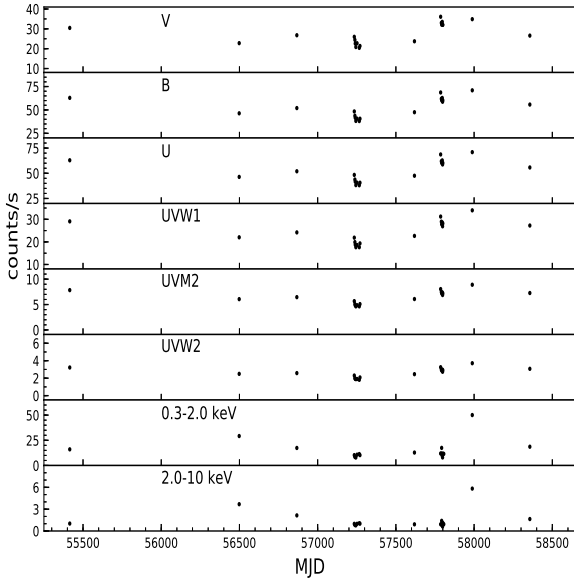


Figure 5. Optical/UV and X-ray long term variability (2010–2018). Going from the uppermost panel to the lowermost, the energies rise from the labeled optical bands through the UV bands to the soft and hard X-ray bands.

m are the variance, corrected for the experimental contribution, and mean of the light curve, respectively) for each light curve (Bhagwan et al. 2016). In Fig. 5, from top to bottom the panels correspond to increasing photon energies. In the X-ray band comparison, the hard band showed a slightly larger amplitude variation compared to the soft band and the variabilities in these energies are 87 per cent, and 66 per cent, respectively. On other hand, all the optical/UV bands show nearly identical flux

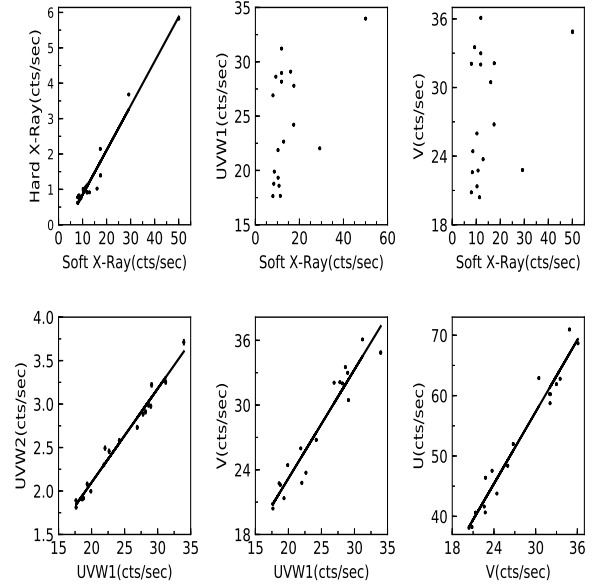


Figure 6. Correlations between several X-ray, optical and UV bands, as labeled on the axes.

Table 4. Variability Correlation parameters between X-ray, Optical and UV bands

Bands	Correlation coefficient	p-value
Soft–Hard X-ray	0.9814	0.0
Soft X-ray–UVW1	0.4804	0.0436
Soft X-ray–V	0.2883	0.2459
UVW1–UVW2	0.9887	0.0
UVW1–V	0.9619	0.0
V–U	0.9785	0.0

variations, with those corresponding to V, B, U, UVW1, UVM2, and UVW2 being 19, 20, 20, 20.5, 20, and 21 per cent, respectively.

We also quantified the correlation between X-ray, optical and UV band variations and an informative subset of those results are plotted in Figure 6. The two X-ray bands are strongly correlated, with coefficient > 0.98 , and comparisons between the UV and optical bands also show strong correlations, with all coefficients > 0.96 . However, there are no significant correlations between the X-ray and UV/optical bands, as shown in Table 4, where we give correlation coefficients and probabilities for the null hypothesis that there is no correlation between them (p-values).

4.3.3 Long Term X-ray Spectral Variability

We next consider the variation of the hardness ratio with time. Seven observations taken from 29 July 2015 to 4 September 2015 have almost the same HR values, so we took an average of these seven HR values for this interval. Similarly, for eight observations taken from 17 August 2016 to 21 February 2017, the HR values are nearly the same and we averaged these eight HR values. By so combining the total of 20 extended observations, we have seven HR versus flux (in 0.3–10 keV) data points, which are shown in Fig. 7.

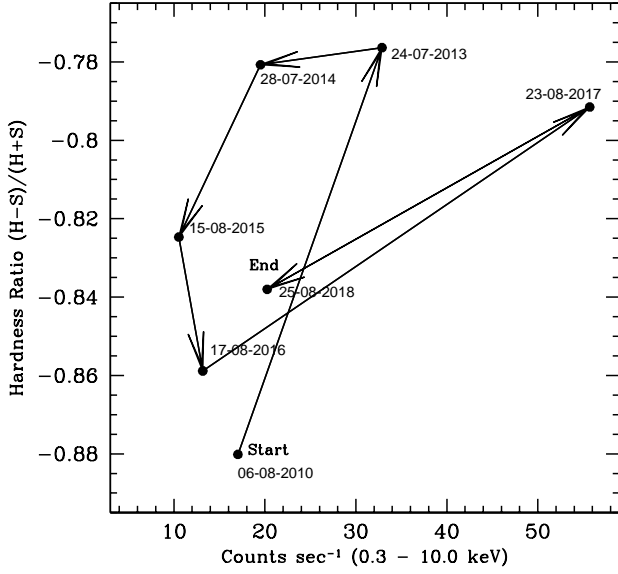


Figure 7. The hardness ratio plotted against flux at different times.

5 DISCUSSION AND CONCLUSIONS

Blazars often evince strong and rapid flux variations across all EM bands and these changes are useful for understanding the emission mechanisms and estimating the sizes, locations, and sometimes even the structure, of the emitting regions in the jets (e.g., Ciprini et al. 2003). There are two fundamental classes of theoretical models that can explain intrinsic AGN emission and variability. Instabilities in or hot spots on accretion discs can explain IDV and STV in radio quiet quasars and in some blazars in low flux states, particularly of the FSRQ class (e.g., Mangalam & Wiita 1993) but this scenario cannot provide a satisfactory explanation for the rapid, robust variations in flux observed from blazars. Relativistic jet based models involving shocks propagating down the jets can explain major LTV (Marscher & Gear 1985; Wagner & Witzel 1995). Weaker fluctuations seen as STV and IDV can be understood in terms of small wiggles in jet direction or helical perturbations (Gopal-Krishna & Wiita 1992; Camenzind & Krockenberger 1992; Pandey et al. 2017), jet turbulence (Marscher 2014; Calafut & Wiita 2015), or a combination of both (Pollack et al. 2016). BL Lac objects have a combination of a featureless optical spectrum with the extreme flux variability and their relativistic jet is very close to the line of sight (LOS) of the observer so the strong Doppler boosting can produce major increments in observed flux along with a reduction in the observed variability timescale (Ulrich et al. 1997).

To estimate an upper limit to the emission region size R , we use the simple causality constraint,

$$R \leq \frac{c t_{var} \delta}{1+z}, \quad (7)$$

where δ is the Doppler factor. The X-ray emission of BL Lacs mostly originates from the jet that is moving at relativistic speeds near the LOS and values of δ for PG 1553+113 have been estimated in previous works. A variability Doppler factor of 11 was found from flaring time scales in 15 GHz radio data (Liodakis et al.

2018), while a larger Doppler factor of between 23 and 35 was estimated through SED fitting with homogeneous one-zone SSC models at different flaring states (Aleksić et al. 2012). Using that range of Doppler factor values, taking $z = 0.433$ (Danforth et al. 2010; Johnson et al. 2019), and employing the shortest variability timescale we found ($t_{var} = 2.4$ ks) in Eqn. (7) above, we obtain that the size of the emission region is in the range of $(0.55 - 1.76) \times 10^{15}$ cm.

The mass of the central SMBH is clearly one of the most fundamental properties of any AGN. In general, spectroscopic techniques involving gas or stellar kinematics and, in particular, reverberation mapping studies, are the most direct and accurate tools for estimating the mass of a SMBH (e.g. Vestergaard 2004). However in case of BL lac objects such as PG 1553+113, these tools cannot be applied due to the lack of emission lines.

Now it is possible that during an X-ray flare, some fluctuations arise that are related to an orbital period of the accretion disc. Then the shortest orbital period timescale and a plausible lower limit to the size of the emitting region would arise close to the last stable orbit around the SMBH. So one can use the minimum variability timescale to estimate the mass of SMBH (Gupta et al. 2009), if the emission arises from the disc, as

$$M/M_{\odot} = 3.23 \times 10^4 \frac{P(s)}{[(r^3/2 + (a/M))(1+z)]}, \quad (8)$$

where a/M is the angular momentum of the BH as a dimensionless parameter between -1 and 1 , r is the minimum radius of the emitting region in terms of the gravitational radius, GM/c^2 , and $P(s)$ is the minimum variability timescale in the flux in seconds. For a non-rotating (Schwarzschild) SMBH ($a = 0$), the innermost circular orbit is $r = 6$. So for the shortest timescale we found of $P = 2.4 \times 10^3$ s and with the redshift of PG 1553+113 ($z = 0.433$) we get an estimate of $\sim 3.7 \times 10^6 M_{\odot}$ for the SMBH. However, for the usually assumed maximally rotating accreting Kerr SMBH, $a = 0.998$ and $r = 1.2$; then the SMBH mass estimate rises to $\sim 2.3 \times 10^7 M_{\odot}$ (e.g., Gaur et al. 2010). However, this estimate is not directly applicable to blazars, where the emission mainly arises from the jets that are launched from very close to the SMBH and not from the accretion disc (Marscher et al. 2008). But if the variability is due to disturbances that originated in the jet but were injected from the accretion disc near the SMBH (e.g., Zhang et al. 2019), then in this case Doppler boosting enhances the variability amplitude by $\sim \delta^3$ and decreases the time scale by δ^{-1} (e.g., Gopal-Krishna et al. 2003). So the mass estimation for the SMBH in PG 1553+113 would rise by a factor of δ , to $\sim 4 \times 10^7 M_{\odot}$, for the Schwarzschild case with the lowest δ (11), up to $\sim 8 \times 10^8 M_{\odot}$ (for the Kerr case and $\delta = 35$). For the following discussion we assume an intermediate value of $\delta = 25$ and take the upper limit to the size of the emitting region and the mass of SMBH to be $\sim 1.3 \times 10^{15}$ cm (from Eq. 7) and $\sim 5.8 \times 10^8 M_{\odot}$ (Eq. 8, for the Kerr case), respectively. It has been argued that PG 1553+113 is a binary SMBH system, with the primary and secondary SMBH masses of $\sim (10^8 - 10^9) M_{\odot}$ and $\sim 10^7 M_{\odot}$ (Ackermann et al. 2015; Tavani et al. 2018) and so this mass estimate is consistent with the primary in that case.

If the fluctuations emerge at a significant distance from the SMBH, then the above approach does not provide clear information about the mass of SMBH. The hard X-ray energy is believed to be generated by synchrotron emission from the HBLs such as

PG 1553+113 and some specific parameters can be estimated. Electrons are likely accelerated within the jet by the diffusive shock acceleration mechanism (Blandford & Eichler 1987) and if this is the case the acceleration timescale in the observer's frame is

$$t_{acc}(\gamma) \simeq 3.78 \times 10^{-7} \frac{(1+z)}{\delta B} \xi \gamma \text{ s}, \quad (9)$$

where B is the magnetic field, γ is the ultrarelativistic electron Lorentz factor and ξ is the acceleration parameter for the electrons. In the observer's frame, the synchrotron cooling timescale of an individual electron having energy $E = \gamma m_e c^2$

$$t_{cool}(\gamma) \simeq 7.74 \times 10^8 \frac{(1+z)}{\delta} B^{-2} \gamma^{-1} \text{ s}. \quad (10)$$

The critical synchrotron emission frequency, in the *XMM-Newton* satellite energy is in the range (Paliya et al. 2015)

$$\nu \simeq 4.2 \times 10^6 \delta (1+z)^{-1} B \gamma^2 = 10^{18} \nu_{18} \text{ Hz}, \text{ where } 0.078 < \nu_{18} < 2.42, \text{ and}$$

$$B \geq 0.12 \nu_{18}^{-1/3} \text{ G}. \quad (11)$$

We estimate the value of electron Lorentz factor to be

$$\gamma \leq 3.5 \times 10^5 \nu_{18}^{2/3}. \quad (12)$$

The relativistic electrons produce photons by Compton scattering in Thomson region and the maximum energy would be (e.g., Pandey et al. 2018):

$$E_{T,max} \simeq \frac{\delta}{(1+z)} \gamma_{max} m_e c^2 \sim 3 \nu_{18}^{2/3} \text{ TeV}. \quad (13)$$

We used the model-independent hardness ratio (HR) analysis to investigate the spectral variations in the X-ray range (0.3–10 keV). It is a simple and efficient way to detect variations in spectra even for relatively low count rates, but does not give any information about physical parameters that could constrain the reasons for the spectral variation. This study showed no significant change in most of the HR plots, but there were two observations in which we found clear increases in the HR as the counts rate increased. Thus PG 1553+113 tends to follow the general harder-when-brighter trend seen in other HSP type blazars (Pian et al. 1998; Zhang et al. 2002; Brinkmann et al. 2003; Pandey et al. 2017).

We used a DCF analysis technique to search for correlations between soft and hard band X-ray emission and we never found a significant time lag between hard versus soft bands, although the count rates were usually insufficient and the variability too modest to yield significant correlations even at zero lag. In general, the X-rays are well correlated in different energy bands (Aggrawal et al. 2018). No time lag has been found in the different energy bands, which is consistent with the emission region being the same for different X-ray energies.

The duty cycle for IDV in the *XMM-Newton* X-ray energy band (0.3–10 keV) is ~ 84 per cent which showed that the source frequently was at least somewhat variable in the lengthy period spanned by these observations (2010–2018). The PSDs of all 20 pointed observations X-ray LCs in this energy range are found to be red-noise dominated, but with a range of spectral slopes, and there is no evidence of a QPO in any of them. Had a QPO signal been detected some interpretation in terms of an origin from a dominant hot-spot on a disc or strong helical features associated with the jet might have been inferred but since QPO signals in

AGN LCs are very rare (and usually short-lived) their absence in these LCs does not preclude any such explanations. The timescales investigated in each observation are too short to constrain any binary black hole model.

The *XMM-Newton* satellite simultaneously conducts observations in the X-ray and optical / UV energy range, helping us to learn some more about the physical process responsible for the emission. This source showed variability in all bands (optical to X-ray) over the long length of these observations. X-ray bands show higher rms variability amplitudes than do the optical and UV bands. We found that the variability amplitude increases with an increase in frequency in X-ray and was essentially constant between the optical/UV bands (with perhaps a slight increase) (Bhagwan et al. 2016). We checked the relations by computing the Pearson correlation coefficients and found good correlations between the optical and UV bands as well as an independent correlation between the soft and hard X-rays which means that their emission region is similar. But as the X-ray fluxes do not correlate significantly with the optical and UV bands, their emission regions should be different.

ACKNOWLEDGEMENTS

We thank the anonymous referee for extensive comments that have led to improvements in the manuscript. This research is based on observations obtained with *XMM-Newton*, an ESA science mission with instruments and contributions directly funded by ESA member states and NASA. HG acknowledges financial support from the Department of Science & Technology (DST), Government of India, through the INSPIRE faculty award IFA17-PH197 at ARIES, Nainital, India.

DATA AVAILABILITY

The data sets were derived from sources in the public domain: [XMM-Newton, <https://heasarc.gsfc.nasa.gov/db-perl/W3Browse/w3browse.pl>]. The data underlying this article will be shared on reasonable request to the corresponding author.

REFERENCES

- Abdo, A. A., Ackermann, M., Ajello, M., et al. 2010a, *ApJ*, 708, 1310
 Abdo, A. A., Ackermann, M., Agudo, I., et al. 2010, *ApJ*, 716, 30, doi:10.1088/0004-637X/716/1/30
 Ackermann, M., Ajello, M., Albert, A., et al. 2015, *ApJ*, 813, L41
 Aggrawal, V., Pandey, A., Gupta, A. C., et al. 2018, *MNRAS*, 480, 4873
 Aharonian, F., Akhperjanian, A. G., Bazer-Bachi, A. R., et al. 2006, *A&A*, 448, L19
 Aharonian, F., Akhperjanian, A. G., Barres de Almeida, U., et al. 2008, *A&A*, 477, 481
 Albert, J., Aliu, E., Anderhub, H., et al. 2007, *ApJ*, 654, L119
 Albert, J., Aliu, E., Anderhub, H., et al. 2009, *A&A*, 493, 467
 Aleksić, J., Anderhub, H., Antonelli, L. A., et al. 2010, *A&A*, 515, A76
 Aleksić, J., Alvarez, E. A., Antonelli, L. A., et al. 2012, *ApJ*, 748, 46
 Aleksić, J., Ansoldi, S., Antonelli, L. A., et al. 2015, *MNRAS*, 450, 4399
 Aliu, E., Archer, A., Aune, T., et al. 2015, *ApJ*, 799, 7
 Bhagwan, J., Gupta, A. C., Papadakis, I. E., et al. 2016, *New Astron.*, 44, 21
 Blandford, R. D., & Rees, M. J. 1978, *Phys. Scr.*, 17, 265
 Blandford, R., & Eichler, D. 1987, *Phys. Rep.*, 154, 1

- Böttcher, M. 2007, *Ap&SS*, 307, 69
- Böttcher, M., Reimer, A., Sweeney, K., et al. 2013, *ApJ*, 768, 54
- Brinkmann, W., Papadakis, I. E., den Herder, J. W. A., et al. 2003, *A&A*, 402, 929
- Calafut, V., & Wiita, P. J. 2015, *Journal of Astrophysics and Astronomy*, 36, 255
- Camenzind, M., & Krockenberger, M. 1992, *A&A*, 255, 59
- Caproni, A., Abraham, Z., Motter, J. C., & Monteiro, H. 2017, *ApJ*, 851, L39
- Ciprini, S., Tosti, G., Raiteri, C. M., et al. 2003, *A&A*, 400, 487
- Danforth, C. W., Keeney, B. A., Stocke, J. T., Shull, J. M., & Yao, Y. 2010, *ApJ*, 720, 976
- Edelson, R. A., & Krolik, J. H. 1988, *ApJ*, 333, 646
- Edelson, R., Turner, T. J., Pounds, K., et al. 2002, *ApJ*, 568, 610
- Falomo, R., & Treves, A. 1990, *PASP*, 102, 1120
- Foschini, L., Ghisellini, G., Tavecchio, F., Bonnoli, G., & Stameria, A. 2011, *A&A*, 530, A77
- Fossati, G., Maraschi, L., Celotti, A., et al. 1998, *MNRAS*, 299, 433
- Fuhrmann, L., Larsson, S., Chiang, J., et al. 2014, *MNRAS*, 441, 1899. doi:10.1093/mnras/stu540
- Gaur, H., Gupta, A. C., Lachowicz, P., et al. 2010, *ApJ*, 718, 279
- Gaur, H., Gupta, A. C., Strigachev, A., et al. 2012, *MNRAS*, 425, 3002
- Ghisellini, G., Villata, M., Raiteri, C. M., et al. 1997, *A&A*, 327, 61
- González-Martín, O., & Vaughan, S. 2012, *A&A*, 544, A80
- Gopal-Krishna, & Wiita, P. J. 1992, *A&A*, 259, 109
- Gopal-Krishna, Sagar, R., & Wiita, P. J. 1993, *MNRAS*, 262, 963
- Gopal-Krishna, Stalin, C. S., Sagar, R., & Wiita, P. J. 2003, *ApJ*, 586, L25
- Green, R. F., Schmidt, M., & Liebert, J. 1986, *ApJS*, 61, 305
- Gupta, A. C., Banerjee, D. P. K., Ashok, N. M., & Joshi, U. C. 2004, *A&A*, 422, 505
- Gupta, A. C., Srivastava, A. K., & Wiita, P. J. 2009, *ApJ*, 690, 216
- Gupta, A. C., Agarwal, A., Bhagwan, J., et al. 2016, *MNRAS*, 458, 1127
- Gupta, A. C., Kalita, N., Gaur, H., et al. 2016, *MNRAS*, 462, 1508
- Hufnagel, B. R., & Bregman, J. N. 1992, *ApJ*, 386, 473
- Johnson, S. J., Mulchaey, J. S., Chen, H.-W. et al. 2019, *ApJ*, 884, 31L
- Kalita, N., Gupta, A. C., Wiita, P. J., Bhagwan, J., & Duorah, K. 2015, *MNRAS*, 451, 1356
- Kataoka, J., Takahashi, T., Makino, F., Inoue, S., Madjeski, G. M., Tashiro, M., Urry, C. M., & Kubo, H. 2000, *ApJ*, 528, 243
- Liodakis, I., Hovatta, T., Huppenkothen, D., et al. 2018, *ApJ*, 866, 137. doi:10.3847/1538-4357/aae2b7
- Mangalam, A. V., & Wiita, P. J. 1993, *ApJ*, 406, 420
- Mannheim, K. 1993, *A&A*, 269, 67
- Marcha, M. J. M., Browne, I. W. A., Impey, C. D., et al. 1996, *MNRAS*, 281, 425
- Marscher, A. P. 2014, *ApJ*, 780, 87
- Marscher, A. P., & Gear, W. K. 1985, *ApJ*, 298, 114
- Marscher, A. P., Jorstad, S. G., D'Arcangelo, F. D., et al. 2008, *Nature*, 452, 966
- Mason, K. O., Breeveld, A., Much, R., et al. 2001, *A&A*, 365, L36
- Max-Moerbeck, W., Hovatta, T., Richards, J. L., et al. 2014, *MNRAS*, 445, 428. doi:10.1093/mnras/stu1749
- Miller, H. R., & Green, R. F. 1983, *BAAS*, 15, 957
- Miller, H. R., Carini, M. T., & Goodrich, B. D. 1989, *Nature*, 337, 627
- Osterman, M. A., Miller, H. R., Campbell, A. M., et al. 2006, *AJ*, 132, 873
- Padovani, P., & Giommi, P. 1995, *MNRAS*, 277, 1477
- Paliya, V. S., Böttcher, M., Diltz, C., et al. 2015, *ApJ*, 811, 143
- Pandey, A., Gupta, A. C., & Wiita, P. J. 2017, *ApJ*, 841, 123
- Pandey, A., Gupta, A. C., & Wiita, P. J. 2018, *ApJ*, 859, 49
- Pandey, A., Gupta, A. C., Wiita, P. J., & Tiwari, S. N. 2019, *ApJ*, 871, 192
- Peterson, B. M., Wanders, I., Horne, K., et al. 1998, *PASP*, 110, 660. doi:10.1086/316177
- Pian, E., Vacanti, G., Tagliaferri, G., et al. 1998, *ApJ*, 492, L17
- Piner, B. G., & Edwards, P. G. 2014, *ApJ*, 797, 25
- Pollack, M., Pauls, D., & Wiita, P. J. 2016, *ApJ*, 820, 12
- Quirrenbach, A., Witzel, A., Kirchbaum, T. P., et al. 1992, *A&A*, 258, 279
- Raiteri, C. M., Stameria, A., Villata, M., et al. 2015, *MNRAS*, 454, 353. doi:10.1093/mnras/stv1884
- Raiteri, C. M., Nicastro, F., Stameria, A., et al. 2017, *MNRAS*, 466, 3762
- Rector, T. A., Gabuzda, D. C., & Stocke, J. T. 2003, *AJ*, 125, 1060
- Reimer, A., Costamante, L., Madejski, G., Reimer, O., & Dorner, D. 2008, *ApJ*, 682, 775
- Romero, G. E., Cellone, S. A., & Combi, J. A. 1999, *A&AS*, 135, 477
- Stocke, J. T., Case, J., Donahue, M., et al. 1991, *ApJ*, 374, 72
- Strüder, L., Briel, U., Dennerl, K., et al. 2001, *A&A*, 365, L18
- Tavani, M., Cavaliere, A., Munar-Adrover, P., & Argan, A. 2018, *ApJ*, 854, 11
- Tiet, V. C., Piner, B. G., & Edwards, P. G. 2012, arXiv:1205.2399
- Ulrich, M.-H., Maraschi, L., & Urry, C. M. 1997, *ARA&A*, 35, 445
- Urry, C. M., & Padovani, P. 1995, *PASP*, 107, 803
- van der Klis, M. 1989, *ARA&A*, 27, 517
- Vaughan, S., Edelson, R., Warwick, R. S., & Uttley, P. 2003, *MNRAS*, 345, 1271
- Vaughan, S. 2005, *A&A*, 431, 391
- Vestergaard, M. 2004, *AGN Physics with the Sloan Digital Sky Survey*, 311, 69
- Wagner, S. J., & Witzel, A. 1995, *ARA&A*, 33, 163
- Zhang, Y. H., Treves, A., Celotti, A., et al. 2002, *ApJ*, 572, 762
- Zhang, Z., Gupta, A. C., Gaur, H., et al. 2019, *ApJ*, 884, 125

SUPPORTING INFORMATION

The online version contains the supporting, supplementary data in the form of extensions to Figs. 1–3.